ACS OMEGA

http://pubs.acs.org/journal/acsodf

Article

Density Functional Theory Study of Ethylene Carbonate Adsorption on the (0001) Surface of Aluminum Oxide α-Al_2O_3

Brian Ramogayana, David Santos-Carballal,* Khomotso P. Maenetja, Nora H. de Leeuw, and Phuti E. Ngoepe*

Cite This: *ACS Omega* 2021, 6, 29577−29587

Read Online

ACCESS | Metrics & More | Article Recommendations

ABSTRACT: Surface coating is one of the techniques used to improve the electrochemical performance and enhance the resistance against decomposition of cathode materials in lithium-ion batteries. Despite several experimental studies addressing the surface coating of secondary Li-ion batteries using α-Al_2O_3, the reactivity of the material toward the electrolyte components is not yet fully understood. Here, we have employed calculations based on the density functional theory to investigate the adsorption of the organic solvent ethylene carbonate (EC) on the major α-Al_2O_3(0001) surface. During adsorption of a single EC molecule, it was found that it prefers to bind parallel to the surface through its carboxyl oxygen. As the surface coverage (θ) was increased up to a monolayer, we observed larger adsorption energies per EC molecule (E_{ads}/N_{EC}) for parallel interactions and a reduction for perpendicular interactions. We also noted that increasing the surface coverage with both parallel and perpendicularly interacting EC molecules led to a decrease of the surface free energies and hence increased stability of the α-Al_2O_3(0001) surface. Despite the larger E_{ads}/N_{EC} observed when the molecule was placed parallel to the surface, minimal charge transfer was calculated for single EC interactions and at higher surface coverages. The simulated scanning tunneling microscopy images are also presented for a clean corundum α-Al_2O_3 surface and after adsorption with different coverages of parallel and perpendicularly placed EC molecules.

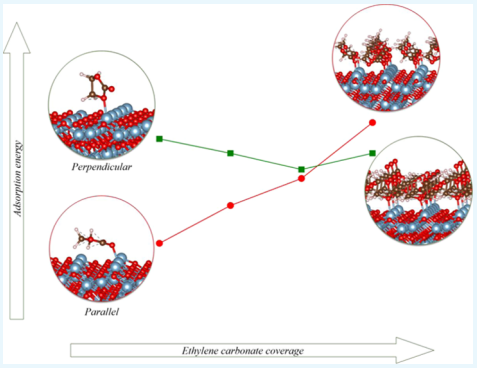

1. INTRODUCTION

Global interest is growing in the development of cheap, renewable, and clean energy storage systems which will facilitate moving away from the reliance on fossil fuels. Alternative energy sources include solar,[1−3] wind,[4,5] and biofuel energy.[6,7] Among the most researched energy storage systems is lithium-ion battery technology, which has application in portable devices, electric vehicles, and stationary smart grids.[8] However, current Li-ion batteries use $LiMn_2O_4$ as a cathode material, which over time needs replacement as it experiences degradation due to the interactions with the electrolyte, which leads to capacity fading.[9−11] Various strategies have been implemented to improve the electrochemical performance of $LiMn_2O_4$, including optimization of the electrolyte,[12,13] using alternative cathode materials[14−17] and electrolyte salts,[18−20] doping the cation sites of the cathode,[21,22] and coating the surface to create an artificial barrier that limits direct cathode−electrolyte contact.[23−27]

Various types of coating materials have been explored, for example, fluorides[28−30] (AlF_3, SrF_2, and LaF_3), phosphates,[31−33] and oxides (ZnO,[34−36] ZrO_2,[37] MgO,[38,39] and Al_2O_3[28−41]), which have shown improved capacity retention and electrochemical performance compared to the uncoated cathode material. Among these, aluminum oxide (α-Al_2O_3) is considered one of the best candidates for coating materials because of its good electrochemical properties.[42] Kannan and Manthiram[43] and Eftekhari[44] initially reported that α-Al_2O_3 significantly improves the electrochemical performance of the $LiMn_2O_4$ spinel at elevated temperatures. Numerous subsequent studies indicated that α-Al_2O_3 also enhances the cycling capacity by reducing the dissolution of the Mn transition metal.[40,41,45−47]

In other technological applications, α-Al_2O_3 is mainly used for its high thermal conductivity, resistance against extreme temperatures and corrosion, and excellent electrical insulation properties.[48−51] Several studies have reported the adsorption of various molecules, including H_2O,[52−54] HCl,[55−57] CO_2,[58] and methanol,[59] onto the α-Al_2O_3 surfaces as these are of interest for different applications. Quan *et al.*[60] employed density

Received: July 15, 2021
Accepted: October 12, 2021
Published: October 29, 2021

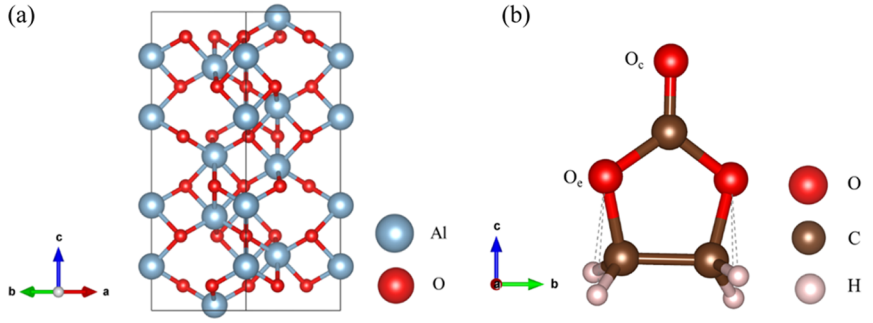

Figure 1. (a) Hexagonal crystal structure of aluminum oxide (α-Al_2O_3) and (b) representation of the EC molecule, indicating the carbonyl (O_c) and ethereal (O_e) oxygen atoms.

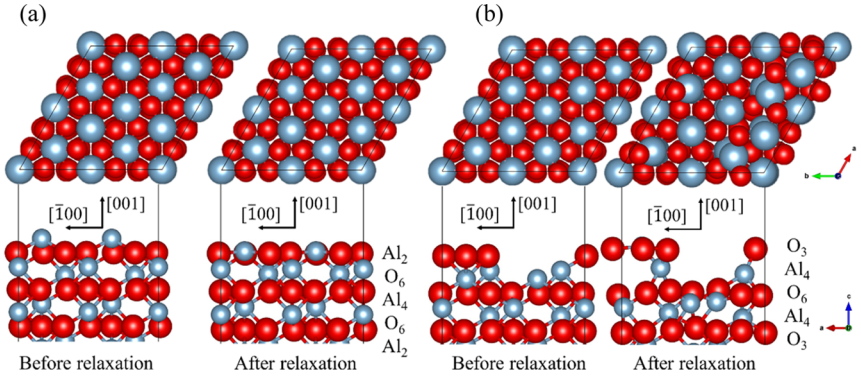

Figure 2. Top and side views of the (a) Al- and (b) O-terminated α-Al_2O_3(0001) surfaces before and after relaxation. The stacking sequence for both Al- and O-terminated surfaces are shown on the far right of each panel. The crystallographic direction for the top view of (0001) surface terminations is [001] for the abscissae toward the right.

functional theory (DFT) simulations to study the adsorption of hydrofluoric acid (HF) on the α-Al_2O_3(0001) surface and found that, upon relaxation, a new Al−F bond was formed. This finding indicates that α-Al_2O_3 creates both a protective barrier on its own between the cathode and the electrolyte components and an additional passivating AlF_3 coating layer following the reaction with the HF acidic electrolyte component.[61]

Ethylene carbonate (EC) is the most stable and effective electrolyte solvent with better electrochemical performance than propylene carbonate, dimethyl carbonate, and diethyl carbonate.[62−64] Compared to other organic solvents, EC has boiling and melting points, which are approximately 248 and 36.4 °C, respectively.[65] In our previous study,[66] we employed DFT calculations with a Hubbard Hamiltonian and long-range dispersion corrections to study the adsorption of EC onto the low-Miller-index surfaces of $LiMn_2O_4$, where we found that the EC weakly adsorbed on the Mn/Li sites of the spinel surfaces *via* the carbonyl or ethereal oxygen, thus allowing the molecule to detach easily to expose the (111) surface. However, the reactivity of EC with the coating material α-Al_2O_3 is equally important but not yet fully understood.

In this paper, we have employed DFT calculations to investigate the reactivity of EC at the major α-Al_2O_3(0001) surface. We discuss the adsorption energies and binding configurations from a single EC molecule up to full monolayer coverage on the α-Al_2O_3(0001) surface. We have also carried out an analysis of the charge transfer and vibrational frequencies and finally have reported calculated scanning tunneling microscopy (STM) images for future comparison with the experiment.

2. RESULTS AND DISCUSSION

2.1. Bulk and Surface Models. The crystal structure of α-Al_2O_3 has hexagonal symmetry with the space group $R\bar{3}c$ (no. 167). The structure consists of a hexagonal close-packed array of oxygen atoms along the [001] direction with the Al atoms occupying two-thirds of the octahedral interstices; see Figure 1a. Following a full bulk optimization, the predicted equilibrium lattice parameters were $a = b = 4.75$ Å and $c = 12.97$ Å, which agrees within 0.21% with the values of $a = b = 4.760$ Å and $c = 12.989$ Å reported in the literature.[76] As shown in Figure 1b, EC is an organic molecule with formula $C_3H_4O_3$ with a high symmetry and large dielectric constant ($\varepsilon \approx 90.5$)[77,78] compared to other organic solvents.

The corundum α-Al_2O_3(0001) surface terminations studied in this work were created by cleaving a fully optimized (2 × 2) supercell of the bulk unit cell using the method implemented in the METADISE code[79] to create nondipolar surface models. We chose to model the α-Al_2O_3(0001) surface, since it has been reported as the dominant plane in corundum nanoparticles.[80−82] The (0001) surface simulation cells contain 120 atoms (48 Al and 72 O) distributed in atomic layers of 6 formula units (f.u.) in both Al- and O-terminated slabs with a surface area of 90.3 Å. A vacuum region of 15 Å was added perpendicularly to the surface termination to avoid interactions between the periodic images. The atoms in the upper layers were allowed to relax (*i.e.*, 3 f.u.), whereas the other atoms in the bottom layers were kept fixed at their relaxed α-Al_2O_3 bulk positions. The two slabs were stoichiometric, symmetric, and nonpolar along the *z*-direction. Figure 2 shows the side and top views of the Al- and O-terminated α-Al_2O_3(0001) surfaces before and after relaxation. Convergence tests were carried out

https://doi.org/10.1021/acsomega.1c03771
ACS Omega 2021, 6, 29577−29587

to determine the required total number of layers, relaxed atomic layers, and the vacuum thickness until the energy change dropped below 1 meV. Dipole corrections perpendicular to the surface plane were applied during our calculations to enhance the convergence of the electronic energy. Geometry optimizations were conducted using the conjugate-gradient technique and were considered converged when the Hellmann−Feynman forces were below 0.01 eV/Å. The stacking sequence of the two terminations consists of alternating Al and O planes, which are reconstructed Tasker type III surfaces.[83] The stoichiometric slab terminating in the Al layer has the sequence Al_2, O_6, Al_4, O_6, ..., O_6, Al_4, O_6, Al_2, and the stacking sequence for the slab terminating in the oxygen layer can be represented as O_3, Al_4, O_6, Al_4, ..., Al_4, O_6, Al_4, O_3.

2.2. Surface Energies. The unrelaxed (γ_u) and relaxed (γ_r) surface energies were calculated using eqs 1 and 2, respectively

$$\gamma_u = \frac{E_{u,slab} - E_{bulk}}{2A} \quad (1)$$

$$\gamma_u + \gamma_r = \frac{E_{r,slab} - E_{bulk}}{A} \quad (2)$$

where $E_{u,slab}$, $E_{r,slab}$, and E_{bulk} are the total energy of the unrelaxed slab, half-relaxed slab, and the bulk, respectively, all with the same number of formula units, whereas A is the surface area of the slab. Unrelaxed surface energies were evaluated from static calculations of a slab created from a freshly cut bulk, while the surface energies of the half-relaxed slabs were calculated after geometry optimization, where the 3 f.u. uppermost atomic layers were allowed to relax, while the remaining bottommost layers were kept fixed at their relaxed bulk positions. The degree of relaxation (R) was also calculated for all surface terminations as

$$R = \frac{\gamma_u - \gamma_r}{\gamma_u} \times 100 \quad (3)$$

As summarized in Table 1, the lowest unrelaxed and relaxed surface energies were obtained for the Al-terminated slab with

Table 1. Surface Energies for the Unrelaxed (γ_u) and Relaxed (γ_r) Al- and O-Terminated α-Al_2O_3(0001) Facets

surface terminations	γ_u (eV/Å^2)	γ_r (eV/Å^2)	R (%)
Al	0.25	0.11	57.0
O	0.38	0.13	65.8

γ_r = 0.11 eV/Å^2, which accounts for the most stable termination. The predominant stability of the Al-terminated (0001) surface is consistent with previously reported studies[54,58,84−87] and the experimental work by McHale *et al.*,[88] who found that γ = 0.16 eV/Å^2. For both Al- and O-terminated surfaces, we observed a large geometry relaxation, with the largest R = 65.8% obtained for the O-terminated slab.

This large difference between the unrelaxed and relaxed surface energies was due to the inward movement of the exposed ions in the Al-terminated facet and an outward ionic movement in the O-terminated slab. During energy minimization, we observed a large relaxation, wherein the Al−O interlayer distance decreased from 1.85 to 1.69 Å and increased from 1.70 to 1.97 Å for the Al-terminated and O-terminated slabs, respectively. This decrease was associated with vertical relaxation of Al−O, wherein the Al-terminated slab experienced an inward relaxation of 0.75 Å along the z-axis, thereby coming closer to the O layer underneath, while the O-terminated slab experienced an outward relaxation of 0.99 Å. Similar findings were previously reported in both experimental and theoretical studies, which also revealed that the Al-terminated surfaces exhibit a large lattice contraction along the z-direction in order to minimize the strong electrostatic attractions.[89−91] Al_2O_3 is a strongly ionic oxide, and the reconstructed surface termination is unstable, since it leaves bare surface Al^{3+} ions or dangling O-bonds.[84,92−95] In this work, the molecular adsorption of EC and the characterization of the physicochemical properties is only performed on the most stable Al-terminated surface, which is the most likely to appear in the corundum crystal morphology in the absence of water.[54]

2.3. Molecular Adsorption. In this section, we study the adsorption of EC on the major Al-terminated α-Al_2O_3(0001) surface. Considering the availability of one top-layer Al site on the (1 × 1) Al-terminated surface, the Al surface sites on our modeled (2 × 2) Al-terminated surface are all identical. The initial EC binding configurations on the surface involve molecular coordination *via* the carbonyl (O_c) and ethereal oxygen (O_e) in parallel, perpendicular, and bridging/bidentate binding orientations. As discussed in our previous work,[66] where the structural parameters of our optimized and isolated EC molecule were compared with the available experimental and theoretical data, our computational settings can properly capture the main properties of this molecule. Upon adsorption, the average adsorption energy per EC molecule on the α-Al_2O_3(0001) surface was calculated as

$$E_{ads} = \frac{1}{N_{EC}}[E_{EC+slab} - (N_{EC}E_{EC} + E_{r,slab})] \quad (4)$$

where $E_{slab+EC}$, and E_{EC} are the total energies of the slab with the adsorbed EC molecules, and the isolated molecule,

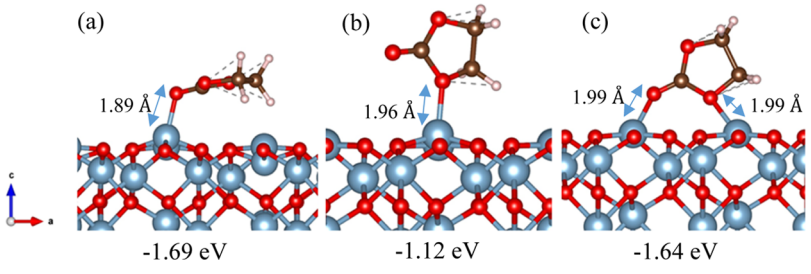

Figure 3. Adsorption energies (E_{ads}) calculated for a single EC molecule placed (a) parallel, (b) perpendicular, and (c) in a bridging/bidentate binding.

https://doi.org/10.1021/acsomega.1c03771
ACS Omega 2021, 6, 29577−29587

respectively. N_{EC} corresponds to the number of adsorbed EC molecules.

2.3.1. Single EC Molecule Adsorption. We next studied the adsorption of a single EC molecule placed parallel and perpendicular to the surface, interacting *via* the carbonyl (O_c), ethereal (O_e) oxygen, and both on the top-layer Al positions of the α-$Al_2O_3(0001)$ surface. In all different orientations, the EC molecule was initially placed at a distance of 2.0 Å from the surface to favor the attractive forces between the adsorbate and the facet. However, the molecule and surface were allowed to move freely during relaxation. Figure 3 summarizes the adsorption energies calculated for the α-$Al_2O_3(0001)$ surface with the EC molecule placed parallel, perpendicular, and in a bridging/bidentate binding. The largest adsorption energy was observed when the molecule was placed parallel to the surface with $E_{ads} = -1.69$ eV. In all adsorptions, the protruding Al atom interacting with the molecule moves upward out of the surface by ∼0.035 Å to form a bond with the EC molecule. Upon relaxation of the bridging/bidentate configuration, the EC molecule preferred to interact with the surface *via* the carbonyl oxygen.

2.3.2. Varying Surface Coverages. To consider the effect of different surface coverages, the number of adsorbed EC molecules (N_{EC}) was increased stepwise until a full monolayer was obtained on the Al-terminated α-$Al_2O_3(0001)$ surface. The surface coverage (θ) was calculated as the ratio between the number of adsorbed EC molecules (N_{EC}) and the total number of available adsorption sites (N) as

$$\theta = \frac{N_{EC}}{N} \tag{5}$$

where $\theta = 0$ indicates that no adsorption takes place on the surface, while $\theta = 1$ shows that the surface adsorption reached a full monolayer. The effect of surface coverage on the average adsorption energy was explored for parallel and perpendicular surface interactions of the EC molecule, which are summarized in Figure 4. Generally, the value of E_{ads}/N_{EC} becomes progressively smaller with N_{EC} for the parallel binding modes, but the average adsorption energy grows for the perpendicular type of orientations for $\theta_{EC} \leq 0.75$, although it slightly decreases again for $\theta_{EC} = 1.00$. The decrease of E_{ads}/N_{EC} observed for the parallel interactions indicates that for $\theta_{EC} > 1$, the steric effects due to the lateral interactions between the EC molecules, which occupy a large surface area, destabilize the system. For perpendicular interactions, the value of E_{ads}/N_{EC} increases with respect to the single EC molecule adsorption up to $\theta_{EC} \leq 0.75$ as there are attractive van der Waals forces between the parallelly stacked molecules. However, we observed a decrease of the average adsorption energy (E_{ads}/N_{EC}) when we reached a full monolayer ($\theta = 1$) as the repulsive steric forces between the closely placed EC molecules become larger than the attractive van der Waals forces. Our results indicate that from a thermodynamic point of view, the EC molecule prefers to attach to the surface in a parallel fashion up to $\theta_{EC} \leq 0.75$, whereas a full monolayer is energetically more favorable if all the molecules change to the perpendicular orientation. We rationalize the change of the adsorption configuration based on steric factors as the parallel molecules repel each other, which therefore need to become perpendicular to the surface to allow better accommodation of the full monolayer. Note that adsorption at higher coverages led to the detachment of the fifth molecule from the surface as it experienced strong steric hindrance caused by the EC−EC interactions.

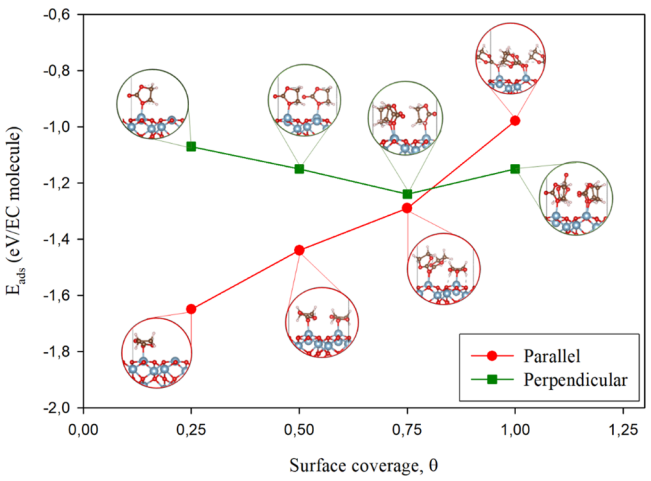

Figure 4. Average adsorption energy as a function of the surface coverage for the EC molecules adsorbed parallelly and perpendicularly to the surface.

We also explored the effect of surface coverage (θ) on the work function (ϕ) for the EC molecules placed in parallel and perpendicular configurations onto the surface. The work function (ϕ) measures the energy required to bring a surface electron into the vacuum,[93] and it is known to be larger for denser surface crystals than for those with open lattices.[96,97] Generally, an increase in the work function was observed as we increase the surface coverage (θ_{EC}) for both parallel and perpendicular interactions; see Figure 5. The largest value of the work function (ϕ) was observed for the full monolayer of perpendicularly placed EC molecules with $\phi = 6.37$ eV.

2.4. Surface Free Energies. We further calculated the surface free energy (σ) for the surfaces after adsorption of different coverages of EC molecules *via*

$$\sigma = \gamma_r + \frac{E_{EC+slab} - E_{r,slab} - N_{EC} \times E_{EC}}{A} \tag{6}$$

Figure 6 summarizes the effect of surface coverage (θ) on the surface free energies (σ). The calculated surface free energies generally decrease compared to the clean surface ($\theta = 0$), indicating that the system is stabilized upon EC adsorption, with the most stable surface achieved when we reach a full monolayer ($\theta = 1$). For parallel interactions, the surface free energies decrease with respect to the surface energy of the pristine (0001) facet up to $\theta \leq 0.75$, when σ stabilizes at around 0.06 eV/Å. At $\theta = 1$, repulsive steric forces between the closely placed EC molecules become larger than the attractive van der Waals forces, and as a result, the fourth molecule detached from the surface upon relaxation of the full monolayer-covered surface, hence leading to the same surface energy for $\theta = 0.75$ and $\theta = 1$ for the parallel EC molecules.

2.5. Bader Charge Analysis. To investigate the electronic charge transfers between the EC molecules and the surface, we carried out a Bader charge analysis for the most favorable adsorption configurations found on the α-$Al_2O_3(0001)$ surface. We used the code developed by Henkelman and collaborators[98] to perform the Bader analysis of charges.[99] In this method, the atoms are defined as the regions enclosed within surfaces of zero flux of charge density. Table 2 summarizes the charge transfers between the surface and the adsorbed EC

https://doi.org/10.1021/acsomega.1c03771
ACS Omega 2021, 6, 29577−29587

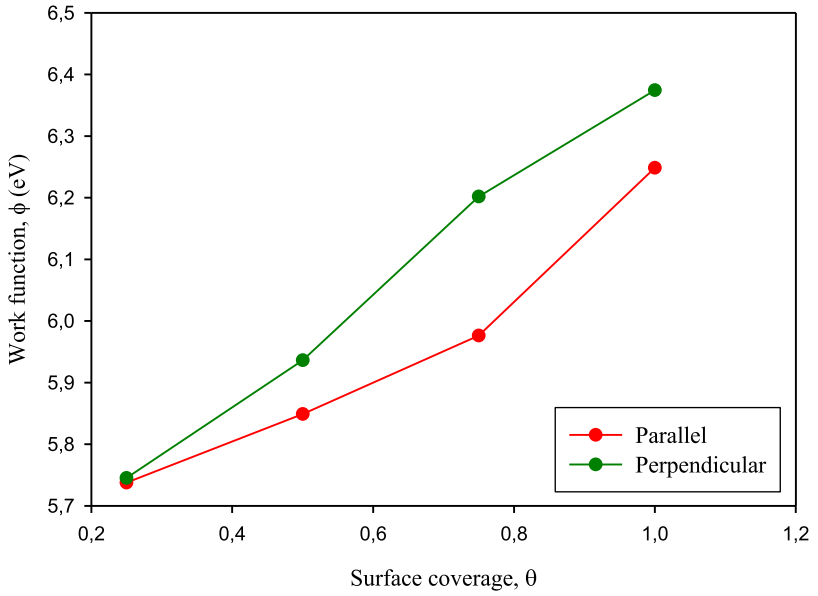

Figure 5. Work function (ϕ) as a function of the surface coverage for the EC molecules adsorbed parallelly and perpendicularly to the surface.

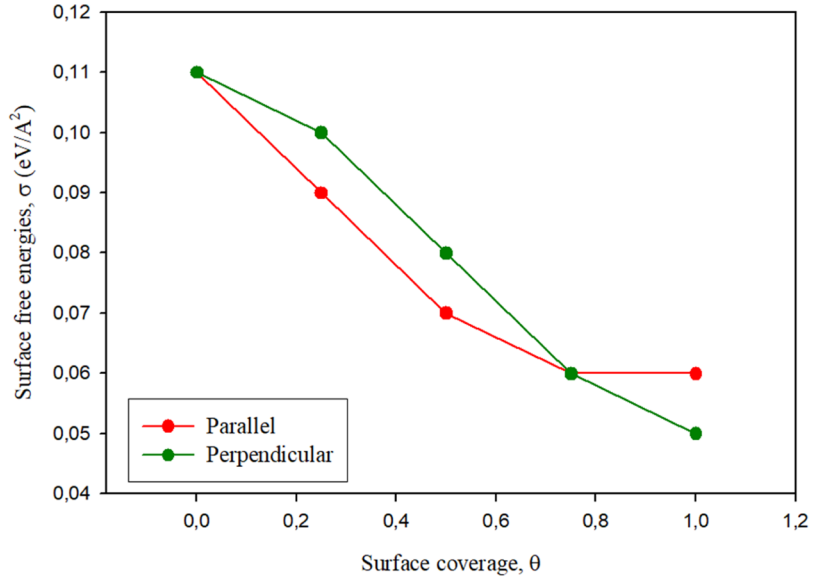

Figure 6. Surface free energies (σ) for the Al-terminated α-$Al_2O_3(0001)$ surface as a function of the surface coverage for the EC molecules adsorbed parallelly and perpendicularly to the surface.

molecules. For the adsorption of a single EC molecule, we generally observed minor charge transfers between the surface and the adsorbate. Similar results were found in our previous study, where we investigated the EC adsorption on the major surfaces of the $LiMn_2O_4$ spinel.[66] The EC molecule gained small charges of −0.094 and −0.071 e^- when it was placed in parallel and perpendicular modes onto the surface. As we increased the surface coverage to θ = 0.50, the charge transfer remained constant in both orientations. However, we found a reduction of the charge transfer for $\theta \geq 0.75$ compared to lower surface coverages of the EC molecule due to the interactions between the closely packed adsorbate molecules. We also calculated the charge accumulation/depletion between the interacting atoms, that is, the carbonyl or ethereal oxygen atoms of the EC molecule and the Al atom of the surface. Our calculations suggest that there is minor charge accumulation for the parallel interactions, whereas there is a minimal depletion of charge for parallel interactions when the coverage is increased up to θ = 0.50. However, we observe a large charge accumulation of 0.761 and 0.836 e^- on the interacting oxygen atom for θ = 0.75 and at full monolayer coverage.

To gain more insights into the electronic charge transfers, we analyzed the differential electron density ($\Delta\rho$). Figure 7 shows the isosurfaces of the electron density difference between the α-$Al_2O_3(0001)$ surface and the EC molecule at different coverages. The charge density difference was obtained by subtracting the sum of the electron charge densities of the clean surface (ρ_{surf}) and an isolated EC molecule (ρ_{EC}), with an identical structure as in the adsorbed form, from the electron density of the total system comprising the surface and the adsorbed molecule (ρ_{sys}) according to

$$\Delta\rho = \rho_{sys} - (\rho_{surf} + \rho_{EC}) \quad (7)$$

https://doi.org/10.1021/acsomega.1c03771
ACS Omega 2021, 6, 29577−29587

Table 2. Charge Transfer between the EC Molecule and the Surface (Δq_{EC}); Average Value for the Charge Accumulation/Depletion within the Interacting EC Atom ($\Delta q_{O_c/O_e}$), *i.e.*, Carbonyl or the Ethereal Oxygen Atom as a Function of the Surface Coverage (θ_{EC})[a] and Average Stretching Mode for the Carbonyl Group ν(C=O), as Well as the Asymmetric $\nu_{asy}(CH_2)$ and Symmetric Stretching Mode $\nu_{sys}(CH_2)$ and the Bending Mode for the Methylene Group $\delta(CH_2)$

					CH_2		
adsorption orientation	θ	Δq_{EC} (e^-)	$\Delta q O_c/O_e$ (e^-)	$\nu_{C=O}$ (cm^{-1})	ν_{sys} (cm^{-1})	ν_{asy} (cm^{-1})	δ (cm^{-1})
	isolated EC molecule			1829	2952	2990	1341
	liquid film EC[66,100]			1803	2928	2955	1397
parallel	0.25	−0.094	−0.053	1654	3087	3022	1482
	0.50	−0.094	−0.049	1665	2991	3112	1474
	0.75	−0.021	0.743	1704	3015	3064	1455
	1.00	−0.010	0.766	1753	3054	3053	1468
perpendicular	0.25	−0.071	0.056	1619	3024	3059	1432
	0.50	−0.072	0.054	1851	3026	3086	1456
	0.75	−0.019	0.617	1819	3091	3040	1465
	1.00	−0.019	0.631	1823	3120	3054	1474

[a]Negative charge transfer values indicate a charge accumulation on the adsorbate, while positive values indicate charge transfers to the surface.

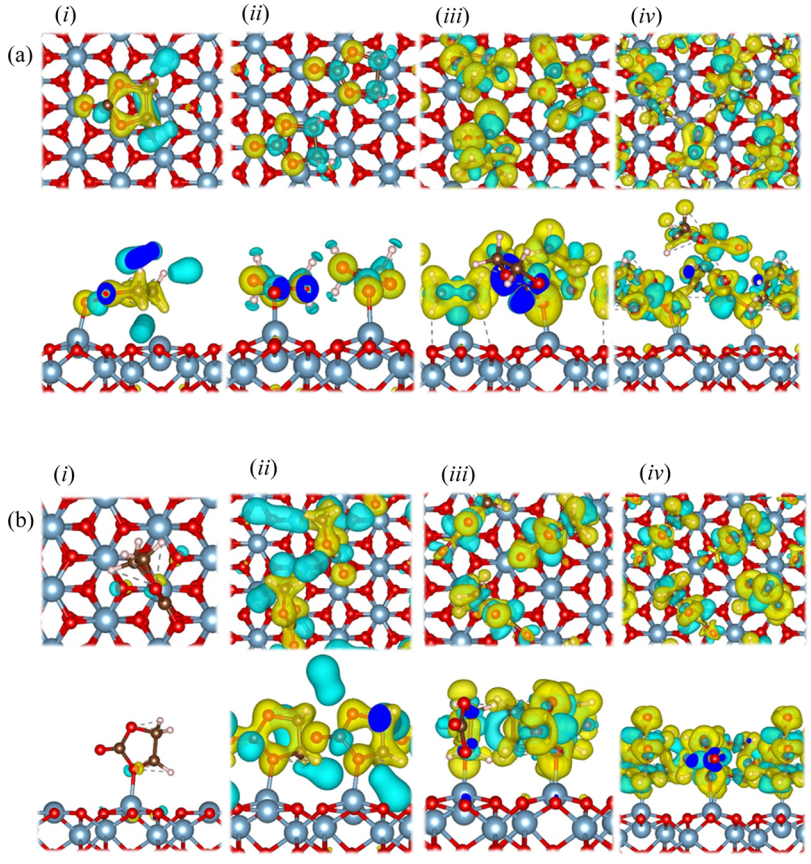

Figure 7. Top and side views of the charge density flow ($\Delta\rho$) for different coverages of the EC molecule adsorbed (a) parallelly and (b) perpendicularly on the α-Al_2O_3(0001) surface. Density gain and depletion regions are represented in yellow and blue, respectively. Isosurfaces display a value of ±0.099, ±0.190, ±0.018, and ±0.009 e/Å^3 for (i) a single EC, (ii) two EC, (iii) three EC, and (iv) four EC molecules.

Figure 7 shows that, although we observe a small charge transfer for the adsorption of a single EC molecule, the electronic charge flow indicates an internal charge rearrangement within the molecule. We observe partial oxidation of the carbon atom and partial reduction of the interacting oxygen due to an intramolecular electronic rearrangement from the C=O π-bond to the newly formed Al−O σ-bond, which is also in agreement with our previous work.[66] The isosurfaces of charge density also indicate electronic accumulation on the hydrogen atoms, caused by the interactions between them and the surface oxygen atoms.

2.6. Vibrational Modes. The simulated wavenumbers of the vibrational modes are directly related to the force constant of the intramolecular bonds, calculated as the second derivatives of the total energy with respect to the atomic positions,[101,102] which were allowed to move by small displacements to ensure that they fall within the harmonic part of the energy potential well. Table 2 summarizes the vibrational modes for the carbonyl group ν(C=O) and

https://doi.org/10.1021/acsomega.1c03771
ACS Omega 2021, 6, 29577−29587

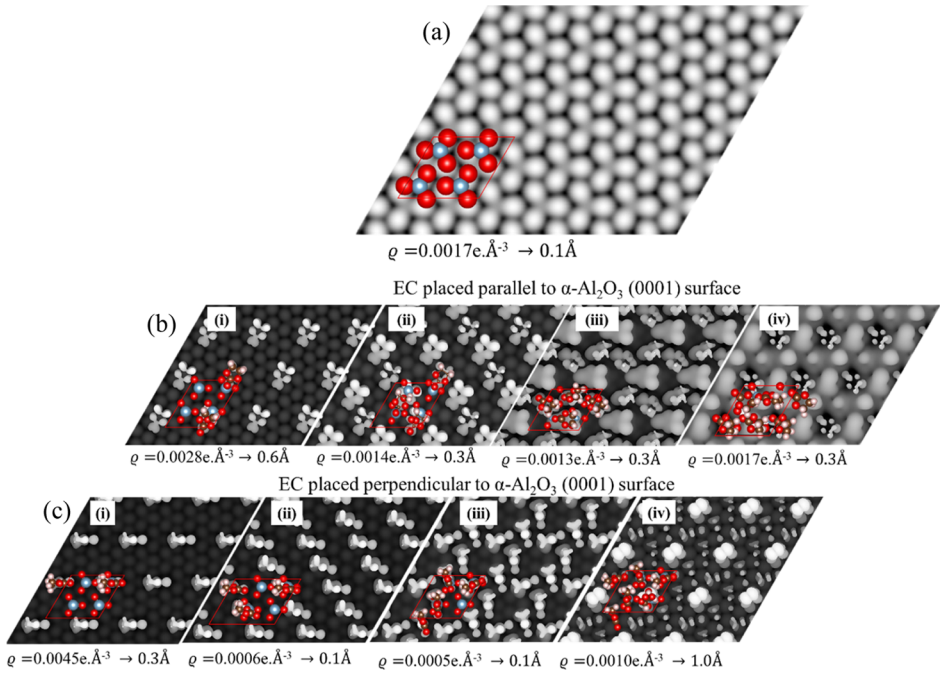

Figure 8. Simulated STM images of (a) clean Al-terminated α-Al_2O_3(0001) surface and after adsorption with different coverages of (b) parallelly and (c) perpendicularly placed EC molecules at a sample bias of −2.5 eV. Density (ϱ) and tip distance (d) are also indicated. Insets show the adsorbed EC molecules and atoms on the top surface layer.

methylene group $\nu(CH_2)$ {*i.e.*, the asymmetric stretching mode (ν_{asy}), symmetric stretching mode (ν_{sys}) and the bending mode (δ)}. The stretching modes presented are the modes for the isolated EC molecule and the average vibrational modes at various EC coverages on the Al-terminated α-Al_2O_3(0001) surface. The wavenumbers of the vibrational modes of an isolated EC molecule are in excellent agreement with the experimental modes for liquid films,[100] and thus, we are confident of our predictions for the interacting molecules. The average stretching modes calculated for EC as we increase the surface coverage remain in the same range as for single EC adsorption, indicating that the vibrational modes are not affected by the increase in coverage. For example, our computed vibrational modes for the carbonyl group ν(C−H) for single adsorptions and at higher coverage were within the range 2850−3300 cm^{-1} reported in the previous studies.[103,104] The carbonyl (C═O) stretching modes are red-shifted compared to the isolated adsorbate, suggesting that the carbonyl double bond weakens upon adsorption. The stretching vibrational modes of the methylene (CH_2) groups are blue-shifted with respect to the isolated EC molecule as a result of the steric effect and the more restricted mobility of the hydrogen atoms.

2.7. STM Images. We have also derived the topographical STM images from a spatial distribution of the valence band state in the vicinity of the Fermi level of the surfaces containing different coverages of the EC molecule. The STM images were simulated according to the basic formulation of the Tersoff−Hamann approach,[105] where the tip of the STM was approximated to an infinitely small point source. We have used the program HIVE[106] for the production of our constant-height STM topographic images, where the partial charge density was integrated between the ranges −2.5 to 0 eV.[107−109] Figure 8 show the STM images for a clean surface and after adsorption with different coverages of parallel and perpendicular EC molecules. The STM for a clean corundum α-Al_2O_3 surface was obtained at 0.1 Å and a density of ϱ = 0.0017 e/$Å^3$, clearly showing alternating rows of well-defined Al and O atoms. The corundum α-Al_2O_3 adopts the same hexagonal array as the isostructural hematite α-Fe_2O_3 mineral, displaying similar STM images.[110−112] STM images for the surfaces with adsorbed EC molecules clearly show the array and orientation of the molecules on the surface, allowing us to discriminate the orientation and surface coverage of the EC molecules. However, due to the size of the molecule, the molecule(s) in the adsorbed surfaces appear as bright spots as shown by the insets. At higher coverage, the images become less clear since the molecules become closely packed and closer to each other.

3. CONCLUSIONS

We have employed DFT calculations to investigate the adsorption of a range of EC coverages onto the major α-Al_2O_3(0001) surface. Our surface energy calculations indicate that the Al-terminated (0001) surface is the most stable facet, which compares well with the previous works. A single EC molecule prefers to bind in a parallel mode to the Al-terminated α-Al_2O_3(0001) surface with only minor charge transfer occurring upon adsorption. When the surface coverage was increased up to the full monolayer, the E_{ads}/N_{EC} for parallel interactions decreased with coverage, whereas the average adsorption energy increased for perpendicular orientations compared to the initial adsorption of an isolated EC molecule. The surface free energies decrease with an increase of the EC coverage, indicating increased surface stability when parallel or perpendicular EC molecules interact with the surface. Minor charge transfers between the surface and EC molecules were generally observed for both orientations even at higher surface coverage. However, we found an increase in charge accumulation on the interacting atom (either the carbonyl or ethereal oxygen). We also observed steric hindrance at higher coverages due to the EC−

https://doi.org/10.1021/acsomega.1c03771
ACS Omega 2021, 6, 29577−29587

EC interaction, which led to the detachment of EC molecules at high coverages.

As we increase the surface coverage, our simulations show an increasing red shift for ν(C═O) with respect to an isolated EC molecule, suggesting that the carbonyl bonds weaken upon adsorptions. The blue shift of the symmetric and asymmetric $\nu(CH_2)$ modes indicate steric hindrance. The simulated STM images are also presented for a clean corundum α-Al_2O_3(0001) surface and surface with adsorbed molecules at different EC coverages. The STM for the clean corundum α-Al_2O_3(0001) surface compares well with the image for the same facet of the isostructural hexagonal haematite α-Fe_2O_3 structure, which can be used for comparison with future experiments.

The results obtained in this work indicate that the EC solvent used as an electrolyte is relatively inert toward Al_2O_3, which is important in the interpretation of the role of alumina as a coating for the cathode materials in Li-ion batteries. Future work will focus on the interaction of EC with the α-Al_2O_3(0001)/$LiMn_2O_4$(111) heteroepitaxial junction and the effect on the mobility of the Li ions through the interface.

4. COMPUTATIONAL METHODS

The spin-polarized DFT calculations were carried out using the Vienna *ab initio* simulation package.[67] The generalized gradient approximation was employed using the Perdew, Burke, and Ernzerhof exchange−correlation functional.[68] The core electrons and their interaction with the valence electrons were described using the projector augmented-wave method[69] in the implementation of Kresse and Joubert.[70] The frozen core electrons comprised levels up to 2p for Al and 1s for O and C, while the electron of the H atom was treated as a valence electron.

The semiempirical method of Grimme with the Becke−Johnson damping [D3-(BJ)][71,72] was included to model the long-range dispersion interactions. The energy of a surface−adsorbate system was also calculated using a number of functionals that include van de Waals interactions,[73,74] but the variation in the calculated results was less than 1%, most likely because the EC molecule is quite polar and the interactions are dominated by electrostatics. The comparison and agreement between these methods shows that the functional chosen in this work [D3-(BJ)] is suitably accurate to describe the surface−adsorbate interactions.

The kinetic energy cutoff was fixed at 560 eV for the expansion of the Kohn−Sham valence states. Γ-Centered Monkhorst−Pack grids of 9 × 9 × 5 and 5 × 5 × 1 *k*-points were used for the integration in the reciprocal space of the α-Al_2O_3 bulk and its two (0001) surface terminations, respectively. The Γ point of the Brillouin zone was sampled during energy minimization of the isolated EC molecule using a cell of dimension 10 Å × 11 Å × 12 Å to avoid spurious interactions. To improve the convergence of the Brillouin zone integrations, Gaussian smearing with a width of 0.05 eV was set for all geometry optimization calculations.[72] However, the tetrahedron method with Blöchl corrections was used to obtain accurate total energies and electronic properties.[75]

AUTHOR INFORMATION

Corresponding Authors

David Santos-Carballal − *School of Chemistry, University of Leeds, Leeds LS2 9JT, U.K.; School of Chemistry, Cardiff University, Cardiff CF10 3AT, U.K.;* orcid.org/0000-0002-3199-9588; Email: D.Santos-Carballal@leeds.ac.uk

Phuti E. Ngoepe − *Materials Modelling Centre, School of Physical and Mineral Sciences, University of Limpopo, Sovenga 0727, South Africa*; Email: phuti.ngoepe@ul.ac.za

Authors

Brian Ramogayana − *Materials Modelling Centre, School of Physical and Mineral Sciences, University of Limpopo, Sovenga 0727, South Africa;* orcid.org/0000-0001-6912-1597

Khomotso P. Maenetja − *Materials Modelling Centre, School of Physical and Mineral Sciences, University of Limpopo, Sovenga 0727, South Africa*

Nora H. de Leeuw − *School of Chemistry, University of Leeds, Leeds LS2 9JT, U.K.; School of Chemistry, Cardiff University, Cardiff CF10 3AT, U.K.; Department of Earth Sciences, Utrecht University, Utrecht 3584 CB, The Netherlands;* orcid.org/0000-0002-8271-0545

Complete contact information is available at: https://pubs.acs.org/10.1021/acsomega.1c03771

Notes

The authors declare no competing financial interest.

ACKNOWLEDGMENTS

The authors acknowledge funding from the UK Economic and Social Research Council (ESRC grant no. ES/N013867/1) and the National Research Foundation South Africa for funding of a UK-SA Newton PhD partnership program. P.E.N. acknowledges the financial support of the DSI-NRF South African Research Chair Initiative, and N.H.d.L. acknowledges the UK Engineering and Physical Sciences Research Council (EPSRC grant EP/K009567) for funding. The authors acknowledge the use of the Centre for High-Performance Computing (CHPC) facility of South Africa in the completion of this work. They also appreciate the support received from DSI Energy Storage Research Development and Innovation Initiative, South Africa. This work was performed using the computational facilities of the Material Modelling Centre (MMC), University of Limpopo, Centre for High-Performance Computing, Cape Town, and the Supercomputing Facilities at Cardiff University operated by ARCCA on behalf of the HPC Wales and Supercomputing Wales (SCW) projects. All data are provided in full in the Results and Discussion section of this paper.

REFERENCES

(1) Motaung, D. E.; Malgas, G. F.; Arendse, C. J.; Mavundla, S. E.; Oliphant, C. J.; Knoesen, D. Thermal-induced changes on the properties of spin-coated P3HT: C60 thin films for solar cell applications. *Sol. Energy Mater. Sol. Cells* **2009**, *93*, 1674−1680.

(2) Raleaooa, P. V.; Roodt, A.; Mhlongo, G. G.; Motaung, D. E.; Kroon, R. E.; Ntwaeaborwa, O. M. Luminescent, magnetic and optical properties of ZnO-ZnS nanocomposites. *Phys. Rev. B* **2017**, *507*, 13−20.

(3) Fan, B.; Zhang, D.; Li, M.; Zhong, W.; Zeng, Z.; Ying, L.; Huang, F.; Cao, Y. Achieving over 16% efficiency for single-junction organic solar cells. *Sci. China: Chem.* **2019**, *62*, 746−752.

(4) Wang, J.; Zhou, S.; Zhang, Z.; Yurchenko, D. High-performance piezoelectric wind energy harvester with Y-shaped attachments. *Energy Convers. Manage.* **2019**, *181*, 645−652.

(5) Fogaing, M. B. T.; Gordon, H.; Lange, C. F.; Wood, D. H.; Fleck, B. A. A Review of Wind Energy Resource Assessment in the Urban Environment. *Advances in Sustainable Energy*; Springer: Cham, 2019; pp 7−36.

(6) Correa, D. F.; Beyer, H. L.; Fargione, J. E.; Hill, J. D.; Possingham, H. P.; Thomas-Hall, S. R.; Schenk, P. M. Towards the implementation of sustainable biofuel production systems. *Renewable Sustainable Energy Rev.* **2019**, *107*, 250−263.
(7) Li, Y.; Tang, W.; Chen, Y.; Liu, J.; Lee, C.-f. F. Potential of acetone-butanol-ethanol (ABE) as a biofuel. *Fuel* **2019**, *242*, 673−686.
(8) Fan, E.; Li, L.; Wang, Z.; Lin, J.; Huang, Y.; Yao, Y.; Chen, R.; Wu, F. Sustainable recycling technology for Li-ion batteries and beyond: challenges and future prospects. *Chem. Rev.* **2020**, *120*, 7020−7063.
(9) Hunter, J. C. Preparation of a new crystal form of manganese dioxide: λ-MnO_2. *J. Solid State Chem.* **1981**, *39*, 142−147.
(10) Dai, Y.; Cai, L.; White, R. E. Capacity fade model for spinel $LiMn_2O_4$ electrode. *J. Electrochem. Soc.* **2012**, *160*, A182.
(11) Bassett, K. L.; Warburton, R. E.; Deshpande, S.; Fister, T. T.; Ta, K.; Esbenshade, J. L.; Kinaci, A.; Chan, M. K. Y.; Wiaderek, K. M.; Chapman, K. W.; Greeley, J. P.; Gewirth, A. A. Operando Observations and First-Principles Calculations of Reduced Lithium Insertion in Au-Coated $LiMn_2O_4$. *Adv. Mater. Interfaces* **2019**, *6*, 1801923.
(12) Sun, X.; Lee, H. S.; Yang, X.-Q.; McBreen, J. Using a boron-based anion receptor additive to improve the thermal stability of $LiPF_6$-based electrolyte for lithium batteries. *Electrochem. Solid-State Lett.* **2002**, *5*, A248−A251.
(13) Li, W.; Lucht, B. L. Inhibition of solid electrolyte interface formation on cathode particles for lithium-ion batteries. *J. Power Sources* **2007**, *168*, 258−264.
(14) Han, D.-W.; Lim, S.-J.; Kim, Y.-I.; Kang, S. H.; Lee, Y. C.; Kang, Y.-M. Facile lithium ion transport through superionic pathways formed on the surface of $Li_3V_2(PO_4)_3$/C for high power Li ion battery. *Chem. Mater.* **2014**, *26*, 3644−3650.
(15) Ouyang, C. Y.; Shi, S. Q.; Wang, Z. X.; Li, H.; Huang, X. J.; Chen, L. Q. Ab initio molecular-dynamics studies on $Li_xMn_2O_4$ as cathode material for lithium secondary batteries. *Europhys. Lett.* **2004**, *67*, 28.
(16) Ledwaba, R. S.; Matshaba, M. G.; Ngoepe, P. E. Molecular dynamics simulations of spinels: $LiMn_2O_4$ and $Li_4Mn_5O_{12}$ at high temperatures. *IOP Conf. Ser.: Mater. Sci. Eng.* **2015**, *80*, 012024.
(17) Mueller, T.; Hautier, G.; Jain, A.; Ceder, G. Evaluation of tavorite-structured cathode materials for lithium-ion batteries using high-throughput computing. *Chem. Mater.* **2011**, *23*, 3854−3862.
(18) Brox, S.; Röser, S.; Husch, T.; Hildebrand, S.; Fromm, O.; Korth, M.; Winter, M.; Cekic-Laskovic, I. Alternative Single-Solvent Electrolytes Based on Cyanoesters for Safer Lithium-Ion Batteries. *ChemSusChem* **2016**, *9*, 1704−1711.
(19) Gao, H.-q.; Zhang, Z.-a.; Lai, Y.-q.; Li, J.; Liu, Y.-x. Structure characterization and electrochemical properties of new lithium salt LiODFB for electrolyte of lithium ion batteries. *J. Cent. South Univ.* **2008**, *15*, 830−834.
(20) Hwang, S.; Kim, D.-H.; Shin, J. H.; Jang, J. E.; Ahn, K. H.; Lee, C.; Lee, H. Ionic Conduction and Solution Structure in $LiPF_6$ and $LiBF_4$ Propylene Carbonate Electrolytes. *J. Phys. Chem. C* **2018**, *122*, 19438−19446.
(21) Michalska, M.; Ziółkowska, D. A.; Jasiński, J. B.; Lee, P.-H.; Ławniczak, P.; Andrzejewski, B.; Ostrowski, A.; Bednarski, W.; Wu, S.-H.; Lin, J.-Y. Improved electrochemical performance of $LiMn_2O_4$ cathode material by Ce doping. *Electrochim. Acta* **2018**, *276*, 37−46.
(22) Kannan, A. M.; Manthiram, A. Surface/Chemically Modified $LiMn_2O_4$ Cathodes for Lithium-Ion Batteries. *Electrochem. Solid-State Lett.* **2002**, *5*, A167−A169.
(23) Guan, D.; Jeevarajan, J. A.; Wang, Y. Enhanced cycleability of $LiMn_2O_4$ cathodes by atomic layer deposition of nanosized-thin Al_2O_3 coatings. *Nanoscale* **2011**, *3*, 1465−1469.
(24) Hao, S.; Wolverton, C. Lithium transport in amorphous Al_2O_3 and AlF_3 for discovery of battery coatings. *J. Phys. Chem. C* **2013**, *117*, 8009−8013.
(25) Park, S.-C.; Kim, Y.-M.; Kang, Y.-M.; Kim, K.-T.; Lee, P. S.; Lee, J.-Y. Improvement of the rate capability of $LiMn_2O_4$ by surface coating with $LiCoO_2$. *J. Power Sources* **2001**, *103*, 86−92.
(26) Lim, S.; Cho, J. PVP-Assisted ZrO_2 coating on $LiMn_2O_4$ spinel cathode nanoparticles prepared by MnO_2 nanowire templates. *Electrochem. Commun.* **2008**, *10*, 1478−1481.
(27) Somo, T. R.; Mabokela, T. E.; Teffu, D. M.; Sekgobela, T. K.; Ramogayana, B.; Hato, M. J.; Modibane, K. D. A Comparative Review of Metal Oxide Surface Coatings on Three Families of Cathode Materials for Lithium Ion Batteries. *Coatings* **2021**, *11*, 744.
(28) Tron, A.; Park, Y. D.; Mun, J. AlF_3-coated $LiMn_2O_4$ as cathode material for aqueous rechargeable lithium battery with improved cycling stability. *J. Power Sources* **2016**, *325*, 360−364.
(29) Li, J.-g.; He, X.-m.; Zhao, R.-s. Electrochemical performance of SrF_2-coated $LiMn_2O_4$ cathode material for Li-ion batteries. *Trans. Nonferrous Met. Soc. China* **2007**, *17*, 1324−1327.
(30) Chen, Q.; Wang, Y.; Zhang, T.; Yin, W.; Yang, J.; Wang, X. Electrochemical performance of LaF_3-coated $LiMn_2O_4$ cathode materials for lithium ion batteries. *Electrochim. Acta* **2012**, *83*, 65−72.
(31) Qing, C.; Bai, Y.; Yang, J.; Zhang, W. Enhanced cycling stability of $LiMn_2O_4$ cathode by amorphous $FePO_4$ coating. *Electrochim. Acta* **2011**, *56*, 6612−6618.
(32) Mohan, P.; Kalaignan, G. P. Structure and electrochemical performance of surface modified $LaPO_4$ coated $LiMn_2O_4$ cathode materials for rechargeable lithium batteries. *Ceram. Int.* **2014**, *40*, 1415−1421.
(33) Zhao, S.; Bai, Y.; Ding, L.; Wang, B.; Zhang, W. Enhanced cycling stability and thermal stability of YPO_4-coated $LiMn_2O_4$ cathode materials for lithium ion batteries. *Solid State Ionics* **2013**, *247*, 22−29.
(34) Tu, J.; Zhao, X. B.; Xie, J.; Cao, G. S.; Zhuang, D. G.; Zhu, T. J.; Tu, J. P. Enhanced low voltage cycling stability of $LiMn_2O_4$ cathode by ZnO coating for lithium ion batteries. *J. Alloys Compd.* **2007**, *432*, 313−317.
(35) Liu, X.; Wang, J.; Zhang, J.; Yang, S. Sol−gel-template synthesis of ZnO nanotubes and its coaxial nanocomposites of $LiMn_2O_4$/ZnO. *Mater. Sci. Eng., A* **2006**, *430*, 248−253.
(36) Aziz, S.; Zhao, J.; Cain, C.; Wang, Y. Nanoarchitectured $LiMn_2O_4$/Graphene/ZnO Composites as Electrodes for Lithium Ion Batteries. *J. Mater. Sci. Technol.* **2014**, *30*, 427−433.
(37) Zhao, J.; Wang, Y. Atomic layer deposition of epitaxial ZrO_2 coating on $LiMn_2O_4$ nanoparticles for high-rate lithium ion batteries at elevated temperature. *Nano Energy* **2013**, *2*, 882−889.
(38) Gnanaraj, J. S.; Pol, V. G.; Gedanken, A.; Aurbach, D. Improving the high-temperature performance of $LiMn_2O_4$ spinel electrodes by coating the active mass with MgO via a sonochemical method. *Electrochem. Commun.* **2003**, *5*, 940−945.
(39) Cai, J.; Lu, M.; Guan, K.; Li, W.; He, F.; Chen, P.; Peng, C.; Rao, P.; Wu, J. Effect of ZnO/MgO ratio on the crystallization and optical properties of spinel opaque glazes. *J. Am. Ceram. Soc.* **2018**, *101*, 1754−1764.
(40) Waller, G. H.; Brooke, P. D.; Rainwater, B. H.; Lai, S. Y.; Hu, R.; Ding, Y.; Alamgir, F. M.; Sandhage, K. H.; Liu, M. L. Structure and surface chemistry of Al_2O_3 coated $LiMn_2O_4$ nanostructured electrodes with improved lifetime. *J. Power Sources* **2016**, *306*, 162−170.
(41) Cho, J.; Kim, Y. J.; Park, B. Novel $LiCoO_2$ cathode material with Al_2O_3 coating for a Li ion cell. *Chem. Mater.* **2000**, *12*, 3788−3791.
(42) Tu, J.; Zhao, X. B.; Cao, G. S.; Zhuang, D. G.; Zhu, T. J.; Tu, J. P. Enhanced cycling stability of $LiMn_2O_4$ by surface modification with melting impregnation method. *Electrochim. Acta* **2006**, *51*, 6456−6462.
(43) Kannan, A. M.; Manthiram, A. Surface/Chemically Modified $LiMn_2O_4$ Cathodes for Lithium-Ion Batteries. *Electrochem. Solid-State Lett.* **2002**, *5*, A167−A169.
(44) Eftekhari, A. Aluminum oxide as a multi-function agent for improving battery performance of $LiMn_2O_4$ cathode. *Solid State Ionics* **2004**, *167*, 237−242.

https://doi.org/10.1021/acsomega.1c03771
ACS Omega 2021, 6, 29577−29587

(45) Kim, W.-K.; Han, D.-W.; Ryu, W.-H.; Lim, S.-J.; Kwon, H.-S. Al_2O_3 coating on $LiMn_2O_4$ by electrostatic attraction forces and its effects on the high temperature cyclic performance. *Electrochim. Acta* **2012**, *71*, 17−21.
(46) Ouyang, C. Y.; Zeng, X. M.; Šljivancanin, Z.; Baldereschi, A. Oxidation states of Mn atoms at clean and Al_2O_3-covered $LiMn_2O_4$ (001) surfaces. *J. Phys. Chem. C* **2010**, *114*, 4756−4759.
(47) Chen, Z.; Qin, Y.; Amine, K.; Sun, Y.-K. Role of surface coating on cathode materials for lithium-ion batteries. *J. Mater. Chem.* **2010**, *20*, 7606−7612.
(48) Arsenault, R.; Fishman, S.; Taya, M. Deformation and fracture behavior of metal-ceramic matrix composite materials. *Prog. Mater. Sci.* **1994**, *38*, 1−157.
(49) French, R. H. Electronic band structure of Al_2O_3, with comparison to Alon and AIN. *J. Am. Ceram. Soc.* **1990**, *73*, 477−489.
(50) Franks, G. V.; Gan, Y. Charging behavior at the alumina-water interface and implications for ceramic processing. *J. Am. Ceram. Soc.* **2007**, *90*, 3373−3388.
(51) Vázquez, B. A.; Pena, P.; De Aza, A. H.; Sainz, M. A.; Caballero, A. Corrosion mechanism of polycrystalline corundum and calcium hexaluminate by calcium silicate slags. *J. Eur. Ceram. Soc.* **2009**, *29*, 1347−1360.
(52) Thomas, A. C.; Richardson, H. H. Growth of Thin Film Water on α-Al_2O_3 (0001): An FTIR Study. *J. Phys. Chem. C* **2008**, *112*, 20033−20037.
(53) Gautier-Soyer, M.; Jollet, F.; Noguera, C. Influence of surface relaxation on the electronic states of the α-Al_2O_3 (0001) surface: a self-consistent tight-binding approach. *Surf. Sci.* **1996**, *352*, 755−759.
(54) de Leeuw, N. H.; Parker, S. C. Effect of Chemisorption and Physisorption of Water on the Surface Structure and Stability of alpha-Alumina. *J. Am. Ceram. Soc.* **1999**, *82*, 3209−3216.
(55) Alavi, S.; Sorescu, D. C.; Thompson, D. L. Adsorption of HCl on single-crystal α-Al_2O_3 (0001) surface: a DFT study. *J. Phys. Chem. B* **2003**, *107*, 186−195.
(56) Nelson, C. E.; Elam, J. W.; Tolbert, M. A.; George, S. M. H_2O and HCl adsorption on single crystal α-Al_2O_3 (0001) at stratospheric temperatures. *Appl. Surf. Sci.* **2001**, *171*, 21−33.
(57) Elam, J. W.; Nelson, C. E.; Tolbert, M. A.; George, S. M. Adsorption and desorption of HCl on a single-crystal α-Al_2O_3 (0001) surface. *Surf. Sci.* **2000**, *450*, 64−77.
(58) Rohmann, C.; Metson, J. B.; Idriss, H. DFT study of carbon monoxide adsorption on α-Al_2O_3 (0001). *Surf. Sci.* **2011**, *605*, 1694−1703.
(59) Borck, Ø.; Schröder, E. First-principles study of the adsorption of methanol at the α-Al_2O_3 (0001) surface. *J. Phys.: Condens. Matter* **2005**, *18*, 1.
(60) Quan, J.-L.; Teng, B.-T.; Wen, X.-D.; Zhao, Y.; Liu, R.; Luo, M.-F. Hydrogen fluoride adsorption and reaction on the α-Al_2O_3 (0001) surface: A density functional theory study. *J. Chem. Phys.* **2012**, *136*, 114701.
(61) Myung, S.-T.; Izumi, K.; Komaba, S.; Sun, Y.-K.; Yashiro, H.; Kumagai, N. Role of alumina coating on Li- Ni- Co- Mn- O particles as positive electrode material for lithium-ion batteries. *Chem. Mater.* **2005**, *17*, 3695−3704.
(62) Xing, L.; Li, W.; Wang, C.; Gu, F.; Xu, M.; Tan, C.; Yi, J. Theoretical investigations on oxidative stability of solvents and oxidative decomposition mechanism of ethylene carbonate for lithium ion battery use. *J. Phys. Chem. B* **2009**, *113*, 16596−16602.
(63) Soetens, J.-C.; Millot, C.; Maigret, B. Molecular dynamics simulation of $Li^+BF_4^-$ in ethylene carbonate, propylene carbonate, and dimethyl carbonate solvents. *J. Phys. Chem. A* **1998**, *102*, 1055−1061.
(64) Van Schalkwijk, W.; Scrosati, B. Advances in Lithium Ion Batteries Introduction. *Advances in Lithium-Ion Batteries*; Springer: Boston, MA, 2002; pp 1−5.
(65) Long, L.; Wang, S.; Xiao, M.; Meng, Y. Polymer electrolytes for lithium polymer batteries. *J. Mater. Chem. A* **2016**, *4*, 10038−10069.
(66) Ramogayana, B.; Santos-Carballal, D.; Aparicio, P. A.; Quesne, M. G.; Maenetja, K. P.; Ngoepe, P. E.; de Leeuw, N. H. Ethylene carbonate adsorption on the major surfaces of lithium manganese oxide $Li_{1-x}Mn_2O_4$ spinel ($0.000 < x < 0.375$): a DFT+U-D3 study. *Phys. Chem. Chem. Phys.* **2020**, *22*, 6763−6771.
(67) Kresse, G.; Furthmüller, J. Efficient iterative schemes for ab initio total-energy calculations using a plane-wave basis set. *Phys. Rev. B: Condens. Matter Mater. Phys.* **1996**, *54*, 11169.
(68) Perdew, J. P.; Burke, K.; Ernzerhof, M. Generalized gradient approximation made simple. *Phys. Rev. Lett.* **1996**, *77*, 3865−3868.
(69) Blöchl, P. E. Projector augmented-wave method. *Phys. Rev. B: Condens. Matter Mater. Phys.* **1994**, *50*, 17953−17979.
(70) Kresse, G.; Joubert, D. From ultrasoft pseudopotentials to the projector augmented-wave method. *Phys. Rev. B: Condens. Matter Mater. Phys.* **1999**, *59*, 1758−1775.
(71) Grimme, S.; Ehrlich, S.; Goerigk, L. Effect of the damping function in dispersion corrected density functional theory. *J. Comput. Chem.* **2011**, *32*, 1456−1465.
(72) Grimme, S.; Antony, J.; Ehrlich, S.; Krieg, H. A consistent and accurate ab initio parametrization of density functional dispersion correction (DFT-D) for the 94 elements H-Pu. *J. Chem. Phys.* **2010**, *132*, 154104.
(73) Klimeš, J.; Michaelides, A. Perspective: Advances and challenges in treating van der Waals dispersion forces in density functional theory. *J. Chem. Phys.* **2012**, *137*, 120901.
(74) Berland, K.; Cooper, V. R.; Lee, K.; Schröder, E.; Thonhauser, T.; Hyldgaard, P.; Lundqvist, B. I. Van der Waals forces in density functional theory: a review of the vdW-DF method. *Rep. Prog. Phys.* **2015**, *78*, 066501.
(75) Blöchl, P. E.; Jepsen, O.; Andersen, O. K. Improved tetrahedron method for Brillouin-zone integrations. *Phys. Rev. B: Condens. Matter Mater. Phys.* **1994**, *49*, 16223−16233.
(76) Ching, W. Y.; Xu, Y.-N. First-Principles Calculation of Electronic, Optical, and Structural Properties of α-Al_2O_3. *J. Am. Ceram. Soc.* **1994**, *77*, 404−411.
(77) Chernyak, Y. Dielectric Constant, Dipole Moment, and Solubility Parameters of Some Cyclic Acid Esters. *J. Chem. Eng. Data* **2006**, *51*, 416−418.
(78) Payne, R.; Theodorou, I. E. Dielectric properties and relaxation in ethylene carbonate and propylene carbonate. *J. Phys. Chem.* **1972**, *76*, 2892−2900.
(79) Watson, G. W.; Kelsey, E. T.; de Leeuw, N. H.; Harris, D. J.; Parker, S. C. Atomistic simulation of dislocations, surfaces and interfaces in MgO. *J. Chem. Soc., Faraday Trans.* **1996**, *92*, 433−438.
(80) Marmier, A.; Parker, S. C. Ab initio morphology and surface thermodynamics of -Al_2O_3. *Phys. Rev. B: Condens. Matter Mater. Phys.* **2004**, *69*, 115409.
(81) Choi, J.-H.; Kim, D.-Y.; Hockey, B. J.; Wiederhorn, S. M.; Handwerker, C. A.; Blendell, J. E.; Carter, W. C.; Roosen, A. R. Equilibrium shape of internal cavities in sapphire. *J. Am. Ceram. Soc.* **1997**, *80*, 62−68.
(82) Kitayama, M.; Glaeser, A. M. The Wulff shape of alumina: III, undoped alumina. *J. Am. Ceram. Soc.* **2002**, *85*, 611−622.
(83) Tasker, P. W. The stability of ionic crystal surfaces. *J. Phys. C: Solid State Phys.* **1979**, *12*, 4977.
(84) Hinnemann, B.; Carter, E. A. Adsorption of Al, O, Hf, Y, Pt, and S atoms on α-Al_2O_3 (0001). *J. Phys. Chem. C* **2007**, *111*, 7105−7126.
(85) Mackrodt, W. C. Atomistic simulation of oxide surfaces. *Phys. Chem. Miner.* **1988**, *15*, 228−237.
(86) Manassidis, I.; Gillan, M. J. Structure and energetics of alumina surfaces calculated from first principles. *J. Am. Ceram. Soc.* **1994**, *77*, 335−338.
(87) Puchin, V. E.; Gale, J. D.; Shluger, A. L.; Kotomin, E. A.; Günster, J.; Brause, M.; Kempter, V. Atomic and electronic structure of the corundum (0001) surface: comparison with surface spectroscopies. *Surf. Sci.* **1997**, *370*, 190−200.
(88) McHale, J. M.; Auroux, A.; Perrotta, A. J.; Navrotsky, A. Surface energies and thermodynamic phase stability in nanocrystalline aluminas. *Science* **1997**, *277*, 788−791.
(89) Meyer, R.; Ge, Q.; Lockemeyer, J.; Yeates, R.; Lemanski, M.; Reinalda, D.; Neurock, M. An ab initio analysis of adsorption and

https://doi.org/10.1021/acsomega.1c03771
ACS Omega 2021, 6, 29577−29587

diffusion of silver atoms on alumina surfaces. *Surf. Sci.* **2007**, *601*, 134−145.
(90) Guenard, P.; Renaud, G.; Barbier, A.; Gautier-Soyer, M. Determination of the α-Al_2O_3 (0001) Surface Relaxation and Termination by Measurements of Crystal Truncation Rods. *Surf. Rev. Lett.* **1996**, *437*, 321−324.
(91) Ruberto, C.; Yourdshahyan, Y.; Lundqvist, B. I. Surface properties of metastable alumina: A comparative study of κ- and α-Al_2O_3. *Phys. Rev. B: Condens. Matter Mater. Phys.* **2003**, *67*, 195412.
(92) Gautier-Soyer, M.; Jollet, F.; Noguera, C. Influence of surface relaxation on the electronic states of the α-Al_2O_3 (0001) surface: a self-consistent tight-binding approach. *Surf. Sci.* **1996**, *352*, 755−759.
(93) Ruberto, C.; Yourdshahyan, Y.; Lundqvist, B. I. Surface properties of metastable alumina: A comparative study of κ-and α-Al_2O_3. *Phys. Rev. B: Condens. Matter Mater. Phys.* **2003**, *67*, 195412.
(94) Verdozzi, C.; Jennison, D. R.; Schultz, P. A.; Sears, M. P. Sapphire (0001) surface, clean and with d-metal overlayers. *Phys. Rev. Lett.* **1999**, *82*, 799.
(95) Jarvis, E. A. A.; Carter, E. A. Metallic Character of the Al_2O_3 (0001)-($\sqrt{31}\times\sqrt{31}$) R±9° Surface Reconstruction. *J. Phys. Chem. B* **2001**, *105*, 4045−4052.
(96) Farkaš, B.; Santos-Carballal, D.; Cadi-Essadek, A.; de Leeuw, N. H. A DFT+ U study of the oxidation of cobalt nanoparticles: Implications for biomedical applications. *Materialia* **2019**, *7*, 100381.
(97) Wang, J.; Wang, S.-Q. Surface energy and work function of fcc and bcc crystals: Density functional study. *Surf. Sci.* **2014**, *630*, 216−224.
(98) Henkelman, G.; Arnaldsson, A.; Jónsson, H. A fast and robust algorithm for Bader decomposition of charge density. *Comput. Mater. Sci.* **2006**, *36*, 354−360.
(99) Laidig, K. E.; Bader, R. F. W. Properties of atoms in molecules: Atomic polarizabilities. *J. Chem. Phys.* **1990**, *93*, 7213−7224.
(100) Matsuyama, S.; Kinugasa, S.; Tanabe, K.; Tamura, T. Spectral Database for Organic Compounds, SDBS; National Institute of Advanced Industrial Science and Technology (AIST), March 31, 1999 [Online]. Available: https://sdbs.db.aist.go.jp/sdbs/cgi-bin/landingpage?sdbsno=2392 [accessed July 24, 2019].
(101) Dzade, N. Y. Computational study of the interactions of small molecules with the surfaces of iron-bearing minerals. Ph.D. Thesis, University College London (UCL), London, 2014.
(102) Santos-Carballal, D. Computational studies of magnetite Fe_3O_4 and related spinel-structures material. Ph.D. Thesis, University College London, London, 2015.
(103) Fortunato, B.; Mirone, P.; Fini, G. Infrared and Raman spectra and vibrational assignment of ethylene carbonate. *Spectrochim. Acta, Part A* **1971**, *27*, 1917−1927.
(104) Allen, J. L.; Borodin, O.; Seo, D. M.; Henderson, W. A. Combined quantum chemical/Raman spectroscopic analyses of Li^+ cation solvation: Cyclic carbonate solvents-ethylene carbonate and propylene carbonate. *J. Power Sources* **2014**, *267*, 821−830.
(105) Tersoff, J.; Hamann, D. R. Theory of the scanning tunneling microscope. *Phys. Rev. B: Condens. Matter Mater. Phys.* **1985**, *31*, 805−813.
(106) Vanpoucke, D. E. P.; Brocks, G. Formation of Pt-induced Ge atomic nanowires on Pt/Ge (001): A density functional theory study. *Phys. Rev. B: Condens. Matter Mater. Phys.* **2008**, *77*, 241308.
(107) Santos-Carballal, D.; Roldan, A.; Grau-Crespo, R.; de Leeuw, N. H. A DFT study of the structures, stabilities and redox behaviour of the major surfaces of magnetite Fe_3O_4. *Phys. Chem. Chem. Phys.* **2014**, *16*, 21082−21097.
(108) Irrera, S.; Roldan, A.; Portalone, G.; de Leeuw, N. H. The role of hydrogen bonding and proton transfer in the formation of uracil networks on the gold (100) surface: a density functional theory approach. *J. Phys. Chem. C* **2013**, *117*, 3949−3957.
(109) Ungerer, M. J.; Santos-Carballal, D.; Cadi-Essadek, A.; van Sittert, C. G. C. E.; de Leeuw, N. H. Interaction of H_2O with the Platinum Pt (001),(011), and (111) surfaces: a density functional theory study with long-range dispersion corrections. *J. Phys. Chem. C* **2019**, *123*, 27465−27476.
(110) Deng, X.; Matranga, C. Selective Growth of Fe_2O_3 Nanoparticles and Islands on Au(111). *J. Phys. Chem. C* **2009**, *113*, 11104−11109.
(111) Condon, N. G.; Leibsle, F. M.; Lennie, A. R.; Murray, P. W.; Parker, T. M.; Vaughan, D. J.; Thornton, G. Scanning tunnelling microscopy studies of α-Fe_2O_3 (0001). *Surf. Sci.* **1998**, *397*, 278−287.
(112) Leibsle, F. M.; Murray, P. W.; Condon, N. G.; Thornton, G. Scanning tunnelling microscopy studies of reactions on metal surfaces and model oxide supports. *J. Phys. D: Appl. Phys.* **1997**, *30*, 741.

https://doi.org/10.1021/acsomega.1c03771
ACS Omega 2021, 6, 29577−29587